Macromolecules

Article

pubs.acs.org/Macromolecules

Polymer-Grafted Nanoparticle Membranes with Controllable Free Volume

Connor R. Bilchak,[†] Eileen Buenning,[†] Makoto Asai,[†] Kai Zhang,[†] Christopher J. Durning,[†] Sanat K. Kumar,*[,†] Yucheng Huang,[‡] Brian C. Benicewicz,[‡] David W. Gidley,[§] Shiwang Cheng,[∥] Alexei P. Sokolov,[∥,⊥] Matteo Minelli,[#] and Ferruccio Doghieri[#]

[†]Department of Chemical Engineering, Columbia University, New York, New York 10027, United States

[‡]Department of Chemistry and Biochemistry, University of South Carolina, Columbia, South Carolina 29208, United States

[§]Department of Physics, University of Michigan, Ann Arbor, Michigan 48109, United States

[∥]Chemical Sciences Division, Oak Ridge National Laboratory, Oak Ridge, Tennessee 37830, United States

[⊥]Department of Chemistry, University of Tennessee, Knoxville, Tennessee 37996, United States

[#]Department of Civil, Chemical, Environmental and Materials Engineering, University of Bologna, 40126 Bologna, Italy

Supporting Information

ABSTRACT: Polymer-based membranes play a key role in several industrially important gas separation technologies, e.g., removing CO_2 from natural gas, with enormous economic and environmental impact. Here, we develop a novel hybrid membrane construct comprised entirely of nanoparticles grafted with polymers. These membranes are shown to have broadly tunable separation performance through variations in graft density and chain length. Computer simulations show that the optimal NP packing forces the grafted polymer layer to distort, yielding regions of measurably lower polymer density. Multiple experimental probes confirm that these materials have the predicted increase in "polymer free volume", which explains their improved separation performance. These polymer-grafted NP materials thus represent a new template for rationally designing membranes with desirable separation abilities coupled with improved aging characteristics in the glassy state and enhanced mechanical behavior.

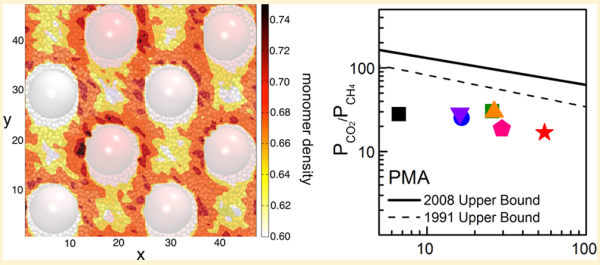

INTRODUCTION

The use of glassy polymer membranes to selectively separate gas mixtures for various applications (e.g., natural gas purification, air separations, carbon capture) is well-established.[1−4] These separations are conventionally achieved through thermodynamic means (e.g., distillation or adsorption), which are both cost and energy-intensive. Membrane separations, on the other hand, require a lower energy demand and are more cost-efficient but are limited by a trade-off between gas permeability (P_i, proportional to product throughput) and selectivity ($\alpha_{ij} = P_i/P_j$, dictates product purity). The inverse correlation between P_i and α_{ij} is now a well-established constraint for these materials, and the current best possible membranes for a given gas separation are captured by the empirical Robeson upper bound.[4−7] Other practical considerations, such as the temporal and mechanical stability of most polymer membrane materials, have also limited their large scale implementation.

In glassy, nonporous polymers the solution-diffusion mechanism controls transport; solute dissolves into the feed-side membrane surface and diffuses through. The material's permeability is then given by the expression $P_i = K_iD_i$, where K_i is the partition coefficient and D_i the diffusion coefficient.[5−9] Glassy polymers are typically diffusion selective; that is, α_{ij} is primarily controlled by the difference in D_i between the two permeating species.

A useful concept here is statistical "free volume", the unoccupied volume in a liquid subject to spatiotemporal fluctuations.[8−11] This is to be distinguished from static microporosity/nanoporosity, i.e., static voids in the material with well-defined, temporally stable geometric characteristics. The difference between these two quantities comes from the fact that free volume in polymer-based materials often arises from inefficient polymer chain packing coupled to local chain dynamics. Free volume is thus thought to be highest in glassy, amorphous polymer systems which possess a stiff backbone with local kinks due to geometric isomerism. It is generally well-accepted that D_i can be manipulated by free volume and/or porosity variations.[12] To date, these changes are almost always achieved by synthetic means,[1,2,8] e.g., synthesis of new

Received: July 6, 2017
Revised: August 30, 2017
Published: September 15, 2017

ACS Publications © 2017 American Chemical Society

DOI: 10.1021/acs.macromol.7b01428
Macromolecules 2017, 50, 7111−7120

polymers with bulky side groups and/or stiff, irregular backbones, which frustrate local packing and affect chain dynamics. Thus, for CO_2/CH_4 separations alone, there have been >300 unique polymers synthesized.[13] For example, poly(trimethyl-1-silyl pentyne) (PTMSP), one of the most permeable polymers studied in the literature, loses up to 90% of its O_2 permeability within 10 days of initial membrane fabrication.[14] Numerous researchers (e.g., Paul et al.) have also examined the effect of aging on membrane permeability and how it depends on the material as well as the sample thickness. This temporal decrease in permeability is known to be directly correlated with a reduction in the free volume available for molecular transport.[15] Underlying all of these important practical limitations is that free volume, and thus permeability, is difficult to systematically tailor in a temporally stable fashion. The stable control of free volume to rationally design membranes thus remains an open challenge.[2,4,8]

It has been well-established that mixed matrix "composite" systems of nanoparticle (NP) filler dispersed in polymer can substantially increase the mechanical strength[16] of the polymer host and limit chain mobility, reducing physical aging.[18] Both of these effects are critical parameters limiting implementation of membranes in industry. In pioneering experimental work, Freeman mooted that the addition of bare NPs to a glassy polymer can also favorably modify the free volume of the polymer.[19,20] This methodology empirically achieves large increases in both P_i and reverse selectivity for CH_4/nC_4H_{10} in poly(4-methyl-1-pentyne) membranes. This result is surprising as conventional composite theory (e.g., Maxwell model) predicts that the permeability decreases with increasing filler volume fraction ϕ, $P_\phi = P_b\left(\frac{1-\phi}{1+\frac{\phi}{2}}\right)$, where P_ϕ and P_b are the permeabilities of the composite and neat polymer, respectively, without affecting selectivity. Freeman et al. propose that their unexpected results arise from additional free volume caused by the incompatibility of the hydrophilic NP and hydrophobic polymer. Unfortunately, NP/polymer incompatibility commonly causes the NP dispersion state to be strongly affected by membrane preparation as well as aging. Paul et al. report very different effects of NP addition on permeability, which appear to be intrinsically linked to the various NP dispersion states obtained from different processing methods.[21] The stability of the NP dispersion can also be significantly affected by the presence of a permeating species in the composite material, which can cause the polymer phase to swell and rearrange. For example, Kaufman et al. have shown that the total number of quantum dot aggregates in a polymer film exposed to chloroform decreased significantly as the loading of chloroform in the composite increased.[22] Other work by Janes shows how the dispersion state of silica NPs in a polymer is altered upon solvent annealing.[23] Thus, while improved performance is sometimes observed, this outcome is not reproducible, controllable, or temporally stable.

Building on these insights, we develop a novel mixed matrix construct composed purely of spherical NPs isotropically grafted with long polymer chains.[24] Our approach is inspired by Baker,[1,2] who suggests that the best hope for transformative improvements in membrane performance is by using novel materials and constructs, including metal−organic frameworks, molecular sieve materials, and mixed matrix membranes. Previous work has established that polymer tethered NPs can crystallize into well-defined ordered arrays, with the grafts filling the space between the cores.[26] Thus, the problem of phase separation between the inorganic NP core and the organic polymer tether is naturally avoided by a phenomenon that is analogous to microphase separation in diblock copolymers.[27,28,29] Computer simulations demonstrate that these systems must reconcile the conflicting drive for the NPs to locally order against the polymer chains having to distort to fill the interstices (see below). This competition evidently creates spatial regions of somewhat lower density over a range of polymer graft densities and chain lengths and thus represents a new paradigm for the precise control of the membrane's free volume and hence its transport properties. Multiple experimental probes of volumetric properties verify this picture and imply that this added free volume in the composites leads to *elevated* permeabilities for both light gases and condensable solutes. Thus, one can manipulate solute permeabilities predictably by varying graft density and chain length. The grafting process is also shown to mechanically reinforce the polymer. Importantly, aging effects for glassy systems are significantly reduced by the presence of the NPs, a significant advantage over conventional synthetic schemes to increase free volume using pure polymers. This new construct therefore offers multiple benefits in the context of gas separation membranes.[2]

MATERIALS AND METHODS

Information and discussion of experiments concerning the glass transition temperatures (T_g) and weight fractions of the composites are included in the Supporting Information. All other experimental and theoretical methods are discussed here.

Grafted NP Synthesis. Poly(methyl acrylate) (PMA) and poly(methyl methacrylate) (PMMA) grafted NPs were synthesized by surface initiated reversible addition−fragmentation chain transfer polymerization (SI-RAFT) technique.[30,31] The RAFT agent 2-(dodecylthiocarbonothioylthio)propanoic acid (DoPAT) was used for the RAFT polymerization. All chemicals were obtained from either Fisher or Acros and used as received unless otherwise specified. Spherical silica nanoparticles (14 ± 4 nm diameter) were obtained from Nissan Chemical. 3-Aminopropyldimethylethoxysilane was purchased from Gelest, Inc. DoPAT was purchased from Boron Molecular, Inc. Methyl acrylate (99%, Acros) and methyl methacrylate (99%, Acros) were purified by filtration through an activated basic alumina column. Azobis(isobutyronitrile) (AIBN) was twice recrystallized from ethanol before use.

A typical example of the polymerization method is described here: DoPAT-NP (0.35 g, 0.43 chains/nm^2) was dispersed in 14 mL of DMF and 7.37 mL of methyl acrylate (0.081 mol). AIBN, dissolved in DMF (0.356 mL, 0.01 M), was added to the solution, and finally the mixture was transferred into a dried Schlenk flask (the methyl methacrylate polymerization followed the literature[31]). The mixture was degassed, backfilled with nitrogen, and then placed in an oil bath at 60 °C. The polymerization solution was quenched in ice water after 2.25 h. THF (20 mL) was added to the flask, and the solution was poured into hexanes (120 mL) to precipitate PMA-grafted nanoparticles. The PMA-grafted silica NPs were recovered by centrifuging at 3000 rpm for 10 min. The nanoparticles were subsequently dispersed in 50 mL of THF and precipitated in 100 mL of methanol. This dispersion−precipitation process was repeated another five times to collect the grafted NPs. The antioxidant Irganox 1010 was added at 0.25 wt % relative to the polymer to minimize oxidation during any subsequent annealing. All solid composites were dried in a covered Petri dish for 2 days, then annealed under vacuum at room temperature for 8 h, and finally under vacuum at either 60 °C (PMA materials) or 150 °C (PMMA materials) for an additional 3 days before any further characterization. All thin-film composites were spin-cast (Laurell Technolgies, North Wales, PA) from 50 to 80 mg/mL THF on to the chosen substrate. The films were then annealed in

DOI: 10.1021/acs.macromol.7b01428
Macromolecules 2017, 50, 7111−7120

the same manner described above. Additional synthesis discussion is provided in the Supporting Information.

^{1}H NMR and ^{13}C NMR (Bruker Avance 300) were conducted using $CDCl_3$ as solvent. Molecular weights and dispersity were determined using gel permeation chromatography (GPC) equipped with a Varian 290-LC pump, a Varian 390-LC refractive index detector, and three Styragel columns (HR1, HR3, and HR4, molecular weight ranges of 100−5000, 500−30 000, and 5000−500 000, respectively). THF was used as eluent for GPC at 30 °C and a flow rate of 1.0 mL/min. The GPC was calibrated with poly(methyl methacrylate) (PMMA) standards obtained from Polymer Laboratories.

Transport Property Measurements. *Steady-State Permeability.* Steady-state permeability of small gases was measured with a constant-volume/variable pressure apparatus described elsewhere.[32] Films of both neat polymers and composite materials with thicknesses ranging between 35 and 50 μm were solvent cast from solutions of 35−50 mg/mL of sample in THF in tall-form Teflon Petri dishes. Films were supported on Celegard 2400 microporous polypropylene with a pore size of 0.04−0.1 μm and 30 μm thick to provide the mechanical stability for the high-pressure measurements. This support provides no appreciable resistance to gas transport. The films were then loaded into the closed-volume apparatus and degassed under vacuum for at least 12 h and exposed to an upstream gas at ≈1.3 bar (gauge). The permeability was calculated from the flux as the gas was allowed to diffuse through the membrane into a downstream chamber of known volume for at least 1 h using the relation $P = \frac{Vl}{RTA\Delta p}\left(\frac{dp_d}{dt}\right)_{t\to\infty}$ where Δp is the transmembrane pressure difference, l is the sample thickness, A is the sample area, V is the volume of the downstream chamber, R is the universal gas constant, and $\frac{dp_d}{dt}$ is the rate of change of the downstream pressure. The temperature, T, was held constant at 35 °C. CO_2, CH_4, and N_2 were tested for Σ = 0.43 chains/nm^2 PMA composites with graft M_n 27, 38, 62, 92, and 132 kDa (nC_4H_{10} was tested for PMA composites with M_n 38, 62, 92, and 132 kDa) in a series of experiments. Neat PMA data were taken from ref 33 for comparison purposes and were independently measured using QCM sorption experiments (see below). Neat PMMA data were taken from ref 7 and also compared with QCM experiments. CO_2 and CH_4 were tested for Σ = 0.44 chains/nm^2 PMMA composites with graft M_n 25, 62, 69, 78, 90, and 114 kDa in a series of experiments.

Unsteady-State Quartz Crystal Microbalance (QCM) Experiments. QCM experiments were performed on thin (<1.5 μm) films of neat polymers and the grafted composites as described previously.[34] QCM measures the resonant frequency of a quartz crystal and monitors its change with mass deposition on the crystal. This can provide direct measurements of both K_i and D_i. We have made use of a QCM with dissipation (QCM-D) to cleanly delineate both the in-phase and loss components of the signal—the in-phase part is used to deduce the mass uptake of the films.

Films were spin-cast onto piranha-cleaned quartz sensors with gold electrodes and known resonant frequencies and annealed under vacuum for 3 days. The coated sensors were then reloaded into the QCM and their resonant frequency measured with the deposited film, effectively "taring" it for use as a microbalance. Gas or vapor penetrants were then flowed over the sensor using a QCM-D equipped with a flow cell (Biolin Scientific, Sweden), and the frequency change of the sensor is monitored throughout the experiment. This provides *in situ* mass uptake measurements of the penetrant in the polymer film. Penetrant flow rates and compositions are controlled using a custom gas handling apparatus equipped with mass flow controllers (Alicat Scientific, Tucson, AZ). Extensive information about the gas handling system, as well as QCM experimental procedure, is provided in the Supporting Information.

Free Volume Measurements. *Positron Annihilation Lifetime Spectroscopy (PALS).* PALS analysis was performed on bulk, dry samples of PMA composites at the University of Michigan. Intensity spectra were fit to a single positronium (Ps) lifetime τ_3 using the software POSFIT. The Ps lifetime and free volume element size can be correlated using the Tau−Eldrup model, which assumes an infinitely deep spherical well where the Ps annihilate with electrons when it is within a short distance of the element surface

$$\frac{1}{\tau_3} = 2\left[1 - \left(\frac{r}{r + r_0}\right) + \frac{1}{2\pi}\sin\left(\frac{2\pi r}{r + r_0}\right)\right]$$

where r_0 is the electron layer thickness, estimated at 0.1656 Å, and r is the radius of the average free volume element. This model is accurate for nanopores (r < 1 nm). Fitting with the rectangular Tau−Eldrup model, which is valid for larger pores, yields similar results.[35]

N_2 Sorption. Specific material surface area and average pore sizes were probed using N_2 adsorption/desorption using a Quantachrome Nova2200E pore size analyzer (Boynton Beach, FL). Approximately 200 mg of the PMA composite samples were dried under vacuum at 25, 75, and 150 °C successively for 1 day at a time to ensure each material was free of any solvent. The samples were then degassed under ultrahigh vacuum (<0.001 mmHg) at 100 °C for 16 h, weighed, and then transferred to the analysis system. Sorption and desorption of N_2 were carried out at liquid nitrogen temperature (77 K). Apparent surface areas are calculated from N_2 adsorption data using the multipoint Brunauer−Emmett−Teller (BET) method,[36] and the pore size distributions are calculated from the N_2 desorption data using the Barrett−Joyner−Halenda (BJH) method.[37]

Density. Densities of the pure polymer and grafted NP composites were measured using an AccuPyc1340 gas pycnometer (Micromeritics, Norcross, GA). Reported densities are an average of at least five independent density measurements, with a uncertainty of <0.15%.

Mechanical and Structural Characterization. *Rheology.* Small-amplitude oscillatory shear (SAOS) measurements in the linear flow regime were conducted over a wide range of temperatures on PMA composites in addition to neat PMA melts of corresponding M_n. The data were collected using an AR2000ex rheometer (T.A. Instruments, New Castle, DE). Samples were dried into cylinders 4 mm in diameter and 1 mm thick. Frequency sweeps between 0.1 and 100 Hz were collected at various temperatures, and master curves were generated using time−temperature superposition.

Electron Microscopy. Transmission electron microscopy (TEM) samples were made by drop-casting solutions of 0.01−0.025 wt % composite in THF onto lacey carbon TEM grids (Electron Microscopy Services, Hatfield, PA). Images were taken on a Libra 120 (Zeiss, Oberkochen, Germany) at the Center for Nanophase Materials Sciences at Oak Ridge National Laboratory (Oak Ridge, TN). Scanning electron microscopy and atomic force microscopy images and procedures are included in the Supporting Information.

SAXS/SANS. Small-angle X-ray scattering (SAXS) measurements were conducted at The University of South Carolina using a SAXSLAB (Amherst, MA) instrument. Small-angle neutron scattering (SANS) experiments were conducted on the CG-2 GP-SANS beamline at Oak Ridge National Laboratory. For SANS, bulk samples of the PMA composites were made via solvent-casting in Teflon dishes followed by thermal annealing in vacuum at 60 °C for 3 days. Dry films of approximately 1.0−1.5 mm in thickness were created by stacking multiple layers of annealed films. Interparticle structure factors $S(q)$ were calculated from the resulting $I(q)$ by dividing by the form factor for polydisperse spheres; these structure factor data were fit with the Percus−Yevick hard sphere model. For SAXS measurements, films of the composite material were spin-cast onto a cleaned silicon wafer from a 10 wt % solution at 1000 rpm for 1 min, yielding a thickness of ∼850 nm. The film was then exposed to successive activities of ethyl acetate while the sample remained in the beam. The ethyl acetate partial pressure was controlled in a manner identical to that used for vapor sorption experiments (see Supporting Information for further details).

Computer Simulations. *Ordered NP Lattice.* We perform coarse-grained molecular dynamics (MD) simulations of polymer-grafted NPs under constant pressure (P) and temperature (T) controlled by the Nosé−Hoover thermostat and barostat. Each nanoparticle of diameter $\sigma_n = 10\sigma$ is grafted with N_c = 200 linear polymer chains of

DOI: 10.1021/acs.macromol.7b01428
Macromolecules 2017, 50, 7111−7120

length $N_p = 10$, where σ is the diameter or a coarse-grained monomer. Any pair of particles i and j at a distance r_{ij} apart, where $i, j \in \{n, p\}$ with n and p indicating nanoparticle and polymer, respectively, interact with each other via the Lennard-Jones (LJ) potential

$$u(r_{ij}) = 4\varepsilon\left[\left(\frac{\sigma}{r_{ij} - \Delta_{ij}}\right)^{12} - \left(\frac{\sigma}{r_{ij} - \Delta_{ij}}\right)^{6}\right], \quad r_{ij} < r_c + \Delta_{ij}$$

where ε and σ set the energy and length scales. We choose $\Delta_{nn} = \sigma_n - \sigma = 9\sigma$, $\Delta_{np} = (\sigma_n - \sigma)/2 = 4.5\sigma$, and $\Delta_{pp} = 0$. The cutoff distance is set at $r_c = 1.12\sigma$ so that the pair potential is purely repulsive. Chain monomers are connected to each other via a finite extensible nonlinear elastic (FENE) bond of strength $K = 30\varepsilon/\sigma^2$ and length $R_0 = 1.5\sigma$.[38] The first monomer of each chain is anchored on the surface of the nanoparticle with a rigid bond. All particles have the same mass m. The LAMMPS simulation package is used with a time step $dt = 0.001\sigma\sqrt{m/\varepsilon}$.[39] The system of $N_n = 32$ polymer grafted NPs are first generated on a dilute face-centered cubic (FCC) lattice. After relaxation of polymer chains at temperature $T = 1.0\varepsilon/k_B$, the FCC lattice is rapidly compressed to the final pressure $P = 2.0\varepsilon/\sigma^3$. The system is then equilibrated for 10^6 time steps at $T = 1.0\varepsilon/k_B$ and $P = 2.0\varepsilon/\sigma^3$.

Single Particle Conformations. We performed MD simulations to clarify the corona structure of isolated polymer-grafted NPs (i.e., a particle in a dilute solution). Each nanoparticle of diameter $\sigma_n = 7\sigma$ is grafted with $N_c = 30$ linear polymer chains of length $N_p = 5$, 10, and 20 in a series of simulations. All interactions follow the LJ potential as discussed above, and hence there are no attractions present in the simulation. We looked for the farthest polymer beads that lay directly at a certain position on the surface and determined the effective radius of this particle at that position on the surface by time averaging for 10^6 time steps at $T = 1.0$. The effective surface was found by repeating this operation for every point on the surface.

RESULTS AND DISCUSSION

We consider steady gas permeation (via the constant volume/variable pressure method) and transient sorption data (via QCM) for transport experiments. We measured the permeability of CO_2, CH_4, nC_4H_{10}, and N_2 in neat PMA, in physical mixtures of PMA and bare spherical silica NPs (14 ± 4 nm in diameter), and in PMA-grafted silica NP membranes. The molecular weight (M_n) and grafting density (Σ) of the PMA grafts are varied in a series of experiments (Supporting Information Tables S1–S5 and Figures S1–S3). Note that the PMA-based materials are above their glass transition temperature, T_g (~15 °C), in these near-ambient experiments ($T = 35$ °C). Keeping in mind that the best membranes for gas separations use glassy polymers, we also studied neat PMMA ($T_g \sim 120$ °C) and PMMA-grafted silica NPs with different M_n ($\Sigma = 0.44$ chains/nm^2). We measured the transport of CO_2 and CH_4 in these glassy materials using linear sorption via the QCM technique. Transport measurements on neat PMA show no discernible M_n dependence. The P_i of the lowest M_n (23 kDa) is nominally 6% larger than that of the highest M_n (135 kDa), essentially within experimental error (5%). Similar results are found for neat PMMA membranes. Physical mixtures of nongrafted NPs and PMA exhibit the decrease in P_i expected from conventional composite theory (see Figure S7).[34,40] In both experimental protocols, films are pinhole- and defect- free across the entire test area.

Light Gas Transport. Figure 1A shows the ideal selectivity of CO_2 over CH_4 as a function of CO_2 permeability in PMA-grafted nanocomposites compared with that of neat PMA. P_i's from free-standing 50 μm thick films of the grafted NPs by steady-state permeation are in quantitative agreement with data

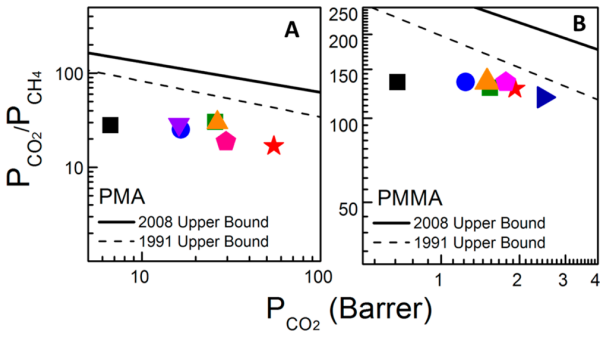

Figure 1. Performance of polymer-grafted NP membranes ($\Sigma = 0.43$ chains/nm^2). Robeson plots comparing the permeabilities of CO_2 and CH_4 in (A) PMA- and (B) PMMA-grafted NP composites for various brush M_n. PMA composites with graft lengths of (blue ●) 27 kDa, (purple ▼) 38 kDa, (pink ⬟) 52 kDa, (green ■) 62 kDa, (red ★) 92 kDa, and (orange ▲) 132 kDa compared with (black ■) neat PMA. PMMA composites with graft lengths of (blue ●) 27 kDa, (green ■) 62 kDa, (pink ⬟) 69 kDa, (purple ▶) 78 kDa, (red ★) 90 kDa, and (orange ▲) 113 kDa compared with (black ■) neat PMMA.

on supported ~0.5–1.5 μm thick films by QCM. These data indicate that permeability is unaffected by thickness in this range.[32,38] Figure 1B shows analogous QCM results from ≈1 μm thick spin-cast films of PMMA grafted NPs. Clearly, the grafted nanocomposites *do not* follow Maxwell's theory, which would predict decreases in permeability and no changes in selectivity, but rather display *enhanced permeability* relative to the corresponding neat polymers. It is important to note that these enhancements occur in both rubbery and glassy materials.

The observed permeability enhancements can be analyzed from two viewpoints. First, the slope of the PMA data on a Robeson plot decreases as the size disparity of the gas pairs becomes larger (Figure 2A, $m_{C_4H_{10}} < m_{CH_4} < m_{N_2}$). The slope of

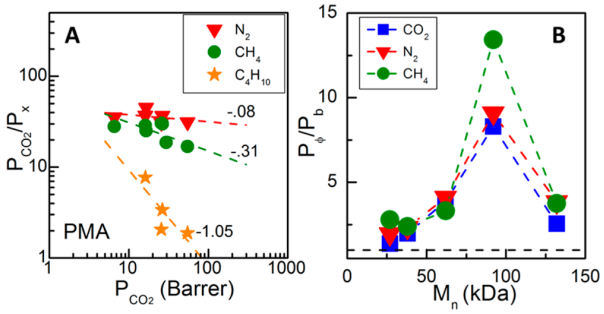

Figure 2. Gas permeability properties of PMA-grafted NPs ($\Sigma = 0.43$ chains/nm^2). (A) Comparison of the slopes of the selectivity/permeability line for CO_2 and three light gases. The slope of the line decreases monotonically as the size disparity between the gas molecules increases; the slope of the CO_2/CH_4 line agrees with literature. (B) Increases in measured gas permeability relative to that of neat PMA (i.e., "volcano plot") for grafted systems. Neat PMA is presented as a dashed line at $P_\phi/P_b = 1$.

CO_2/CH_4 data (−0.31) is in good agreement with literature values of the upper bound slope for this gas pair (−0.30). It has been theorized previously[6] that the upper bound slope is related to the relative sizes of the gas molecules being considered; this serves as an indication that the grafted NP

DOI: 10.1021/acs.macromol.7b01428
Macromolecules 2017, 50, 7111–7120

membranes are separating the gas pairs based on size sieving and not on solubility differences.

Furthermore, the enhancements in P_i can be controlled effectively by variations in chain length. Figure 2B shows a nonmonotonic trend ("volcano plot") for permeability as a function of PMA graft M_n at a fixed grafting density (Σ = 0.43 chains/nm^2) for CO_2, N_2, and CH_4. nC_4H_{10} also shows the same trends, and similar results are found for the PMMA analogues (Figure S14). As an illustrative example, we focus on the relative permeability, P_ϕ/P_b, of CO_2. The permeability of grafted NP composites with short chains (<50 kDa) shows a distinct increase when compared to the pure polymer and the Maxwell model (which predicts $P_\phi/P_b \leq 1$ for all M_n), with the degree of enhancement increasing with M_n. P_ϕ/P_b then increases substantially at intermediate chain lengths, before decreasing at large chain lengths. However, these large chain length materials still have $P_\phi/P_b > 1$, indicating they are more permeable than pure PMA. The PMA composite displaying the maximum permeability in this series (i.e., M_n = 92 kDa) is the same for all four gases and shows about an order of magnitude increase relative to the pure polymer; for example, P_{CO_2} = 56.1 ± 0.1 barrer in the most permeable PMA composite, but it is only 6.7 ± 0.15 barrer in the pure PMA (see Figure S13).

Figure 1A further shows that there are only minor changes in selectivity of CO_2 over CH_4 even when the CO_2 permeability increases by nearly an order of magnitude; For example, P_{CO_2}/P_{CH_4} of the most permeable composite deceases by ≈35% when P_{CO_2} increases by over 800%. Similar results are found for the PMMA systems (Figure 1B), where P_{CO_2}/P_{CH_4} appears to be even less affected. The selectivity of CO_2 over N_2 is also unaffected across the same range in CO_2 permeability in the PMA composites (Figure 2A and Figure S4). Evidently, these grafted NP composites exhibit unexpected shifts to the "right" on the Robeson plot when M_n changes, toward the upper bound, with the best PMMA system nearly on top of the 1991 upper bound.[7]

Note that these materials are competitive with commercial cellulose acetate membranes with respect to CO_2 permeance, a measure of permeability that has been normalized to the thickness of the material being considered. For example, a 500 nm thick PMA composite film with M_n = 92 kDa has a permeance of 115 GPU, which is comparable to that of commercial cellulose acetate (≈100 GPU).[41]

Permeability Enhancement Driven by Free Volume. The "volcano" shape of relative permeability versus PMA graft M_n at fixed Σ = 0.43 chains/nm^2 (Figure 2B) is remarkably similar to trends observed for the free volume element size from positron annihilation lifetime spectroscopy (PALS, Figure 3A and Figure S5).[17,19,20] The lateral size for the PALS-derived free volume "elements" is 4−5 Å, comparable to the Kuhn length of the polymers, consistent with the local fluctuating nature of this free volume metric. The apparent connection between enhanced free volume and "static" excess volume is supported by room temperature pycnometry, which is used to compute the excess volume $\tilde{V}$ relative to volume additivity:

$$\tilde{V} = \frac{1}{\rho_c} - \frac{\omega_{NP}}{\rho_{NP}} - \frac{\omega_{poly}}{\rho_{poly}}$$

where ω is the weight fraction, ρ is the density, and the subscripts c, NP, and poly denote the composite, nanoparticle, and polymer, respectively. Despite the large relative error

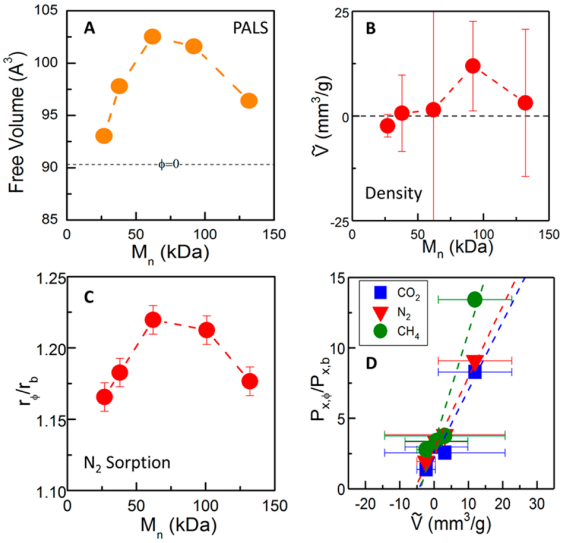

Figure 3. Free volume metrics for PMA-grafted NP composites (Σ = 0.43 chains/nm^2). (A) Measured free volume element size from PALS experiments as a function of the composite brush M_n. The volume size clearly displays a nonmonotonic M_n dependence. (B) Excess volume $\tilde{V}$ computed from pycnometry experiments. $\tilde{V}$ can be related to fractional free volume, FFV (see Supporting Information). (C) Relative apparent pore sizes (r_i) in composites from N_2 isotherms. The pore size increases found from sorption and free volume element sizes measured from PALS are strongly correlated (see Supporting Information). (D) Correlation between relative gas permeability increases and $\tilde{V}$ for the three light gases examined (Figure 2B).

arising from uncertainty in ω_{NP}, it is clear that the intermediate chain length systems have the largest excess volume (Figure 3B). Since the excess volume is related to the fractional free volume (FFV),[19] the data indicate that intermediate M_n composites possess the highest amount of FFV (Figure S23).

This excess volume can also be indirectly probed using N_2 adsorption isotherm data at 77 K, where the material is glassy. With the caveats that this measurement is sensitive to sample preparation and to the amount of time the sample is held at 77 K during the measurement, this provides a measure of the frozen, static pore size in the medium. Presumably, this is related to the pycnometry data in the room-temperature liquid state. The PMA composites clearly exhibit higher apparent pore sizes and surface areas from BET model fits (Figure 3C and Figure S15D), again implicating volume increases. Indeed, the excess volume from pycnometry and macroscopic gas permeabilities are linearly correlated (Figure 3D). Each of these facts supports the hypothesis that free volume changes result in the permeability enhancements seen in the polymer-grafted NP membranes.[8,19]

Condensable Penetrant Experiments. Linear sorption measurements using the QCM apparatus allow for the independent measurement of K_i and D_i in supported films in the thickness range 300−1500 nm, much closer to thicknesses used in industrial applications than those used in permeation experiments. Experiments that directly measure both K_i and D_i can also provide insight as to how these properties are altered in the different NP composites, and their individual contributions to the observed permeability increase. Figure 4 shows results for a condensable solute, ethyl acetate, in PMA composites with Σ = 0.43 chains/nm^2 at fixed penetrant partial

DOI: 10.1021/acs.macromol.7b01428
Macromolecules 2017, 50, 7111−7120

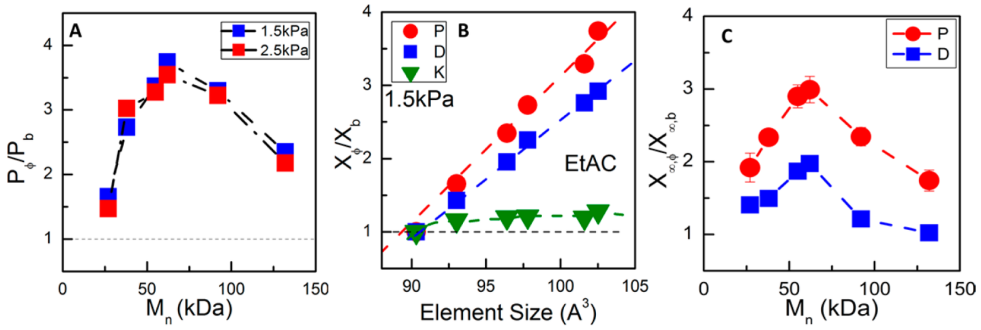

Figure 4. Transport properties for a condensable solute in PMA composites. (A) "Volcano plot" of relative permeability of ethyl acetate as a function of M_n at various partial pressures. (B) Correlation of P_ϕ/P_b (red ●), D_ϕ/D_b (blue ■), and K_ϕ/K_b (green ▼) for ethyl acetate versus free volume element size as measured by PALS for a single experimental partial pressure. (C) Relative increase of P_i and D_i at infinite dilution for ethyl acetate as a function of PMA graft M_n.

pressures (additional grafting densities and partial pressures are in the Supporting Information, Figures S6–S12). As with the light gases, the permeability of ethyl acetate in the grafted system is elevated relative to neat PMA (and the Maxwell prediction) for low M_n (Figure 4A). As PMA M_n increases, a prominent maximum in permeability is seen with $P_\phi/P_b \approx 4$ at intermediate M_n (62 kDa). For larger M_n, the relative permeability decreases but remains above the neat polymer. We find that K_i is increased by only ~30% independent of M_n, indicating somewhat enhanced sorption in these elevated free volume structures, but that the chain length does not appear to have any significant effect. By contrast, the D_i increases by a factor of ≈3, qualitatively similar to the trends observed for P_i (Figures S9B and S9C, respectively). This indicates that the permeability enhancements seen here are a direct result of elevated diffusion. Analogous with the P_i from the light gas permeation, we find excellent correlation between the "free volume element" size, in this case derived from PALS, and P_i and D_i (Figure 4B). Importantly, the data indicate that the increase in relative permeability is primarily due to changes in D_i, consistent with permeability enhancement via free volume. Extrapolation of P_i and D_i to the infinite dilution limit (Figure 4C) shows the same trends and clearly indicates that the changes observed reflect an inherent membrane property and not a solute concentration effect. This implies that the composite materials are natively more permeable than the corresponding neat polymer, a fact that is supported by the increased free volume as measured by PALS and excess volume measured by pycnometry. This is also consistent with the slope of the CO_2/CH_4 Robeson line in Figure 2A, which argues against solubility-driven effects.

Characterizing Rheological and Mechanical Properties. Linear rheology on the PMA composites with the same grafting density and various M_n allows us to understand the polymer's mechanical response and how it is affected by the presence of the NPs. For large PMA graft M_n (132 kDa), the composites behave qualitatively similar to the neat polymer with the corresponding M_n over the frequency range examined (Figures 5A, Figures S16 and S17). This is expected based on the relatively low loading of well-dispersed silica NPs (ϕ = 0.04).[15] As M_n decreases, important differences in mechanical behavior emerge. A pronounced "elongation" of the rubbery plateau appears for moderate M_n (77 kDa, Figure 5B), implying that the material is behaving more like a solid at lower frequencies; i.e., the silica cores begin to dominate the

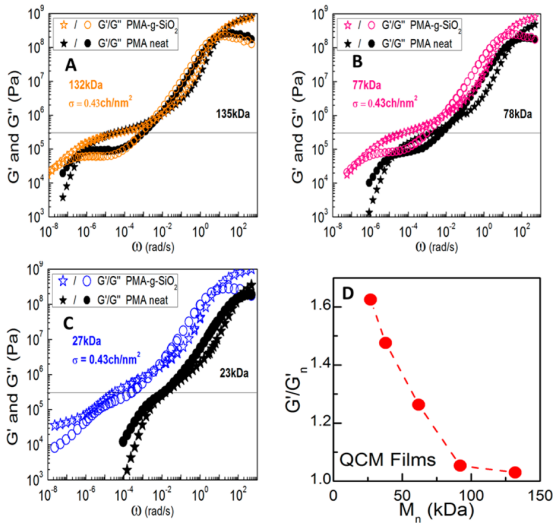

Figure 5. Mechanical reinforcement of bulk and thin film PMA composites. Time–temperature superposition master curves of SAOS rheology (reference temperature = 20 °C) plotting G' (☆/★) and G'' (○/●) as a function of frequency, ω, of (A) 132 kDa/135 kDa, (B) 77 kDa/78 kDa, and (C) 27 kDa/23 kDa for PMA-grafted NP composites (Σ = 0.43 chains/nm^2) (open colored symbols)/neat PMA (solid black symbols), respectively. (D) Reinforcement of the composite shear modulus for thin films (≈900 nm) from QCM data.

dynamics. At M_n = 27 kDa, the material is clearly solid-like, as evidenced by the slow decay of the modulus at low frequency (Figure 5C). In fact, at the lowest measured frequency, the modulus is ≈20 kPa. This crossover to soft-gel-like behavior for polymer-grafted NP systems has been observed by many workers.[15,42]

QCM data on dry composite films provide the "glassy" modulus G_ϕ measured at much higher frequency (≈5 MHz). Neat PMA with M_n = 65 kDa yields $G_b \sim 2$ GPa, consistent with extrapolations of lower frequency linear rheology data to this regime. These results are in good agreement with recent reports that films as thin as 100 nm exhibit mechanical properties that are equivalent to bulk samples.[16] All the polymer grafted composites have elevated values of G_ϕ/G_b (see Figure 5D). Evidently, the NPs serve to beneficially reinforce the mechanical properties of these constructs across all frequencies, independent of film thickness down to 300 nm.

DOI: 10.1021/acs.macromol.7b01428
Macromolecules 2017, 50, 7111–7120

Aging Effects. Importantly, we find no measurable effects on CO_2 permeability despite aging for up to 10 weeks for the PMMA composites (Figure 6A). This is in contrast to the

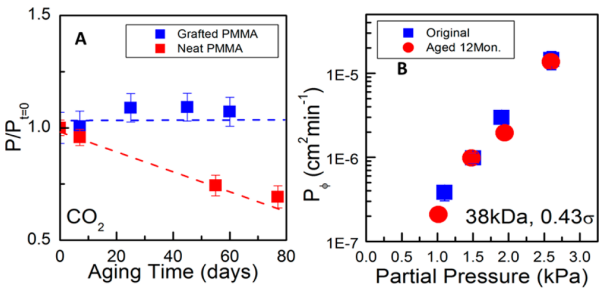

Figure 6. Aging of neat and NP composite polymer films. (A) Effect of aging time on CO_2 permeability in neat PMMA and in a PMMA-grafted NP composite with M_n = 62 kDa and Σ = 0.44 chains/nm^2. (B) Time dependence of ethyl acetate permeability in a PMA-grafted composite. Additional time points and samples are shown in the Supporting Information.

permeability of CO_2 in neat PMMA, which decreases by up to 25% in the 10 week time frame. These data show that performance degradation in glassy PMMA can be significantly reduced when the chains are grafted to NPs. This has important practical implications for polymer membrane materials that have superior transport properties but undergo severe aging, such as PIMs and TR polymers.

Figure 6B illustrates that the PMA grafted NP systems show no aging effects in the presence of the ethyl acetate for up to 1 year. Additional aging experiments (Supporting Information) show that the permeability of similar PMA-grafted NP composites (Σ = 0.07 chains/nm^2) remains constant for up to 2 years. This result in rubbery materials is particularly interesting due to the tendency of ethyl acetate and other condensable penetrants to cause significant structural rearrangement in physical mixtures of NP and PMA, which may alter transport properties.[23] This provides evidence that the NP composite materials are stable in the presence of large mass loadings (~10 wt %) of solvent. Chemical stability such as this is advantageous in many industrial membrane applications, including methanol/MTBE vapor separations and robustness against contaminant poisoning.[2]

Morphology. A series of microscopy and scattering studies were performed on both the neat PMA materials and their NP grafted analogues to discern the structure and packing of the NPs. Transmission electron microscopy (TEM, Figures 7A–C and Figure S18) and small-angle neutron scattering (SANS, Figure 7D and Figure S21) of composites of various M_n suggest local NP ordering in the range of chain lengths studied, but not true crystallization. The SANS scattering intensities are modeled by a product of a Percus–Yevick structure factor (modeling NP packing effects) and a polydisperse sphere form factor to represent the individual NPs. While most of the samples show one broad peak, the 132 kDa sample's inter-NP spacing is large enough that two peaks, corresponding to the first two reflections, are clearly visible. The scattering peaks can also be seen shifting to lower q-values, corresponding to larger interparticle distances, as the brush M_n increases. This is in qualitative agreement with the increasing NP spacing seen in the TEM images.

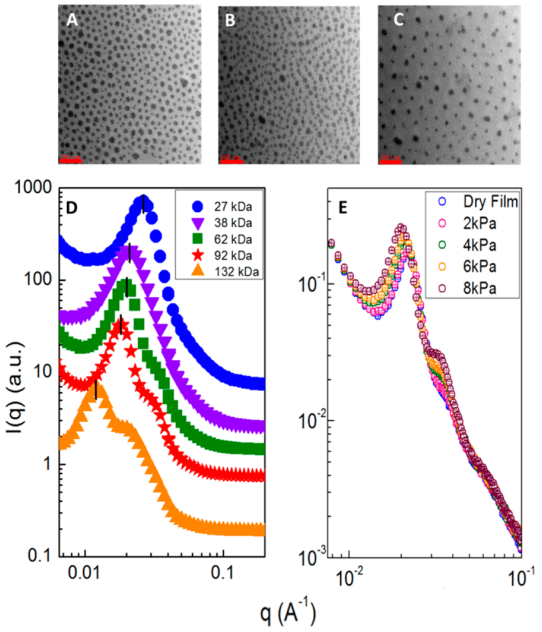

Figure 7. Structural characterization of polymer-grafted NPs. (A–C) In-plane TEM micrographs of PMA-grafted NPs (Σ = 0.43 chains/nm^2) with M_n of (A) 27, (B) 62, and (C) 132 kDa. Samples were prepared by drop-casting onto TEM grids. The scale bar is 100 nm in all images. (D) SANS absolute intensity, $I(q)$, as a function of PMA graft M_n for Σ = 0.43 chains/nm^2 (curves shifted vertically for clarity). The peak position gives the inverse of the inter-NP separation from which the mean brush height can be derived. (E) SAXS intensity for a composite film (M_n = 55 kDa) swollen under increasing ethyl acetate partial pressure. The magnitude and location of the scattering features increase proportionally with ethyl acetate partial pressure, indicating an "affine" expansion of the nanocomposite upon swelling. This indirectly confirms a uniform structure free of defects or voids. Data are not shifted vertically.

Hansen[43] has suggested that the first peak of the interparticle structure factor, defined as the measured intensity signal divided by the measured form factor of the bare NPs (see Supporting Information), exceeds 2.85 in crystalline samples. Our fitted values of ≤1.91 are well below this value. Thus, while there is short-ranged hexatic NP packing, there is no long-range order, possibly due to the polydispersity of silica cores (d = 14 ± 4 nm). The SANS-derived height of the brush layer (see Supporting Information, eq S11) varies with $\sqrt{M_n}$ as expected at a fixed grafting density.[45] Interestingly, the most significant enhancement in transport characteristics occurs when the brush height is comparable to the size of the NP core: at M_n = 92 kDa the brush height is 9 nm, comparable to the radius of the NP (7 ± 2 nm). As discussed previously, this may provide a design criterion for optimizing the transport properties of these membrane constructs. Other researchers have also found similar unusual properties of polymer-grafted NPs when the thickness of the grafted polymer is comparable to the size of the NP.[24,44]

Previous experiments on arrays of polymer grafted NPs using confocal laser scanning microscopy,[45] SAXS and SANS,[46] X-ray reflectivity,[47] and in-plane and cross-sectional transmission TEM[48,49] show that these materials are uniform and have no measurable NP aggregation and no observable pinholes. Our own in-plane TEM (Figure 4A–C and Figure S18), scanning

DOI: 10.1021/acs.macromol.7b01428
Macromolecules 2017, 50, 7111–7120

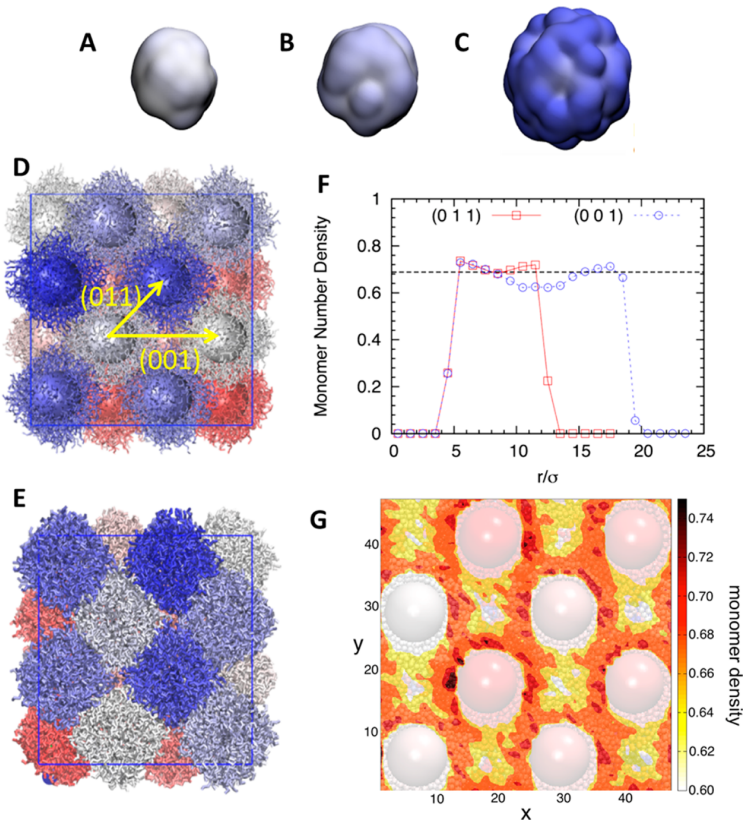

Figure 8. Computer simulations of polymer-grafted NPs. (A–C) Coarse-grained computer simulation results of grafted nanoparticles for (A) short (N = 5), (B) medium (N = 10), and (C) long (N = 20) chain lengths (30 chains per particle); particle diameter = 7, monomer size = 1. (D, E) Coarse-grained molecular dynamics simulations of polymer grafted nanoparticle assemblies highlighting the polymer corona distortion from an isotropic spherical shell to allow for filling space. The particle diameter is 10, and the monomer size is 1. 200 chains of 10 monomers are uniformly grafted to each particle, and the particle initial positions are fixed. (D) highlights the NP core, while (E) highlights the polymer corona. (G) Monomer density histogram corresponding to the corona in (D) and (E), showing the chain density dependence in the (001) and (011) directions. The x-axis is radial distance away from the particle core (r), normalized to the size of the particle (σ). (G) "Heatmap" of monomer density in NPs (diameter = 10) grafted with polymer chains (monomer diameter = 1, chain length = 10, 200 chains per particle, averaged over 500 simulations). The interstitial regions in the structure have moderately reduced polymer density relative to the rest of the corona structure.

electron microscopy (Figure S19), and atomic force microscopy (Figure S20) are consistent with these conclusions. SAXS experiments comparing the dry samples to samples swollen with ethyl acetate lend support to this conclusion (Figure 7E). Two important points are noted. If the samples had any significant porosity, we expect that the solvent-induced swelling would fall below that implied by the amount of solvent adsorbed. Instead, we find that the interparticle spacing changes by ≈7% (seen as the first peak in $I(q)$ shifts to lower q) when the sample imbibes ≈20% solvent, essentially ruling out such voids. Second, we can fit the SAXS data with two scattering lengths—one for the NP core and the other corresponding to a homogeneous mixture of polymer and solvent. Independent SANS data, where we use different compositions of mixtures of ethyl acetate and its perdeuterated analogue, verify these findings. Together, these facts argue against the presence of microscopic pores in these samples. This is in contrast to literature on membranes with controlled microporosity but agree with previous studies on grafted NP composites.[45−49] This realization, combined with the free volume measurements above, indicates the enhancement of free volume without introducing porosity. Since free volume is a dynamically changing quantity representative of molecular motion, while porosity is generally thought of as a measure of static voids or pores within a material, we would not expect porosity to necessarily increase as the free volume in a polymer increases. For example, TR polymers can have fractional free volumes of over 20% and free volume sizes of ∼5 Å, yet are still not considered to be microporous in nature (i.e., the solution-diffusion model of transport is still applicable).

Simulations. To further support the proposed free volume picture, we simulated isolated polymer-grafted NPs using a coarse-grained model. Figures 8A–C show a series of ensemble averaged conformations of single particles (diameter = 7, monomer diameter = 1) with 30 chains each with chain lengths of (A) 5, (B) 10, and (C) 30 monomers. If we were to naively scale both the NP size and the brush size to be commensurate with the experiments, then these simulations would correspond to PMA M_n of 40, 130, and 300 kDa at a fixed graft density of Σ = 0.7 chains/nm^2, which is higher than the experimental graft densities discussed in this study. Figure 8C shows that for sufficiently long grafted chain lengths the corona appears isotropic, which presumably facilitates crystallization. This can be seen in the corresponding TEM image of high-M_n grafts and in the presence of an additional scattering peak (Figures 7C and 7D, respectively). In contrast, the NPs with shorter chain

DOI: 10.1021/acs.macromol.7b01428
Macromolecules 2017, 50, 7111−7120

length grafts have asymmetric corona shapes. This lack of isotropy likely prevents long-range structure formation, as observed experimentally. It is important to note that these singe particle conformations are performed in the absence of any other particles (i.e., the particles are in dilute solution) and will not necessarily represent the conformation of the polymer corona in the presence of other NPs.

To investigate the polymer corona structure at higher NP concentrations, we also simulated multi-NP systems where the NPs are initially placed on a dilute face-centered-cubic (FCC) lattice. The simulation snapshots shown here are composed of 200 polymer chains, each with 10 monomers, grafted onto a NP with a diameter of 10 monomers. Figure 8D highlights the NP cores, which have been placed and held in an FCC structure. Ongoing studies are relaxing this assumption and are allowing the NPs to form the structures that they prefer—the results of this more sophisticated analysis are deferred to future work. To accommodate this NP packing, the grafted coronas are forced to assume anisotropic shapes to fill the interstitial spaces and attempt to maintain a uniform polymer density (Figure 8E). In fact, the corona shape is consistent with the Wigner−Seitz cell of the FCC lattice, namely a rhombic docadecahedron. Thus, chains located along the [011] direction are compressed, while chains along the [001] direction stretch to fill the interstitial space between the spherical cores. Figure 8F shows monomer density profiles as a function of radial distance away from the center of a particle core, expressed in units of monomer size σ. Monomers near the surface of the particle (for example, at $\sigma = 5$) appear to have densities similar to that of the simulated neat polymer melt. However, the monomer density is reduced along the [001] direction near the lattice interstices (at distances of $10 < \sigma < 15$). This is consistent with the polymer chains stretching in this direction. This corona distortion, which results from a compromise between NP ordering and chain packing, increases the free volume, as shown in the corresponding "heatmap" of monomer density generated as an average of 500 independent simulation snapshots (Figure 8G). Since density has been shown to be related to free volume,[20] these regions of decreased density should lead to free volume increases. This is corroborated by the experimentally measured densities of the composites (Figure 3B). The combination of the PALS free volume experiments, multi-NP simulations, and experimental and computational density calculations argues that the free volume in grafted NPs can be suitably controlled to enhance material permeability while also increasing the chemical, mechanical, and temporal stability of the polymer brush.

CONCLUSIONS

The chemical grafting of polymer chains to inert NPs is a novel design platform for advanced polymeric membranes. This material platform permits precise tuning of gas permeabilities and selectivities through the polymer graft characteristics, both above and below T_g. Evidently, statistical free volume is directly manipulated by the grafts. Importantly, we find no deleterious aging effects in glassy materials and in addition to mechanical reinforcement of the polymer phase. While the performance improvements found for these polymer-grafted NP membranes are significant, there are other glassy polymers even better suited for particular separations.[4,17,25] The NP-grafted analogues of these newer polymer classes might provide a rational means of designing even better membranes, exceeding the Robeson limit. Work to graft chains with such chemistry to NPs is currently underway. It is important to note that the use of these novel materials in gas separation membrane modules demands fabrication of thin layers (<100 nm) on a porous support. This could possibly be accomplished by a number of well-known protocols (e.g., spin/dip/spray coating). Such efforts will be part of our future work in this area.

ASSOCIATED CONTENT

Supporting Information

The Supporting Information is available free of charge on the ACS Publications website at DOI: 10.1021/acs.macromol.7b01428.

Figures S1−S24 (PDF)

AUTHOR INFORMATION

Corresponding Author

*E-mail sk2794@columbia.edu (S.K.K.).

ORCID

Connor R. Bilchak: 0000-0001-8815-1601
Kai Zhang: 0000-0001-9700-7943
Sanat K. Kumar: 0000-0002-6690-2221
Yucheng Huang: 0000-0002-2367-6199
Brian C. Benicewicz: 0000-0003-4130-1232
Shiwang Cheng: 0000-0001-7396-4407

Author Contributions

C.R.B. and E.B. contributed equally to this work as co-first authors.

Notes

The authors declare no competing financial interest.

ACKNOWLEDGMENTS

Partial financial support for this work was provided by the National Science Foundation Graduate Research Fellowship Program (EB: grant # DGE-11-44155; CRB: grant #DGE-16-44869), the NSF DMREF program (CBET-16929502(SK)) and DMR-1507030 (SK,KZ). This material is partially based upon work supported by the U.S. Department of Energy, Office of Science, Office of Workforce Development for Teachers and Scientists, Office of Science Graduate Student Research (SCGSR) program (EB). The SCGSR program is administered by the Oak Ridge Institute for Science and Education for the DOE under Contract DE-AC05-06OR23100. B.C.B. and Y.H. acknowledge support from the SC SmartState program. The SANS results were performed at Oak Ridge National Laboratories (grant # IPTS-13903.1). SAXS experiments were performed through the South Carolina SAXS Collaborative, supported by the NSF Major Research Instrumentation program (Award #DMR-1428620). S.C. and A.P.S. acknowledge support by DOE, Office of Science, Basic Energy Sciences, Materials Science & Engineering Division. Some of this work was initiated when F.D. was visiting Columbia University—we thank the University of Bologna and Columbia University for partially supporting this visit. E.B. and C.R.B. thank Dr. Dustin Janes for his assistance with QCM experiments. E.B. thanks Jiahua Zhu for assistance with transmission electron microscopy and Halie Martin for assistance with pycnometry experiments.

REFERENCES

(1) Baker, R. W.; Lokhandwala, K. Natural gas processing with membranes: An overview. *Ind. Eng. Chem. Res.* **2008**, *47*, 2109−2121.

DOI: 10.1021/acs.macromol.7b01428
Macromolecules 2017, 50, 7111−7120

(2) Baker, R. W.; Low, B. T. Gas Separation Membrane Materials: A Perspective. *Macromolecules* **2014**, *47*, 6999−7013.
(3) Robeson, L. M.; Liu, Q.; Freeman, B. D.; Paul, D. R. Comparison of transport properties of rubbery and glassy polymers and the relevance to the upper bound relationship. *J. Membr. Sci.* **2015**, *476*, 421−431.
(4) Robeson, L. M. The upper bound revisited. *J. Membr. Sci.* **2008**, *320*, 390−400.
(5) Lin, H. Q.; Freeman, B. D. Materials selection guidelines for membranes that remove CO_2 from gas mixtures. *J. Mol. Struct.* **2005**, *739*, 57−74.
(6) Freeman, B. D. Basis of permeability/selectivity tradeoff relations in polymeric gas separation membranes. *Macromolecules* **1999**, *32*, 375−380.
(7) Robeson, L. M. Correlation of Separation Factor versus Permeability for Polymeric Membranes. *J. Membr. Sci.* **1991**, *62*, 165−185.
(8) Ramesh, N.; Davis, P. K.; Zielinski, J. M.; Danner, R. P.; Duda, J. L. Application of Free-Volume Theory to Self Diffusion of Solvents in Polymers Below the Glass Transition Temperature: A Review. *J. Polym. Sci., Part B: Polym. Phys.* **2011**, *49*, 1629−1644.
(9) Vrentas, J. S.; Duda, J. L. Diffusion in polymer—solvent systems. I. Reexamination of the free-volume theory. *J. Polym. Sci., Polym. Phys. Ed.* **1977**, *15*, 403−416.
(10) Cohen, M. H.; Turnbull, D. Molecular transport in liquids and glasses. *J. Chem. Phys.* **1959**, *31*, 1164−1169.
(11) Fujita, H. Diffusion in polymer-diluent systems. *Adv. Polym. Sci.* **1961**, *3/1*, 1−47.
(12) Park, J. Y.; Paul, D. R. Correlation and prediction of gas permeability in glassy polymer membrane materials via a modified free volume based group contribution method. *J. Membr. Sci.* **1997**, *125*, 23−39.
(13) Huang, Y.; Paul, D. R. Physical aging of thin glassy polymer films monitored by gas permeability. *Polymer* **2004**, *45* (25), 8377−8393.
(14) Consolati, C.; Genco, G.; et al. Positron annihilation lifetime (PAL) in poly [1-(trimethyl-silyl) propine](PTMSP): free volume determination and time dependence of permeability. *J. Polym. Sci., Part B: Polym. Phys.* **1996**, *34* (2), 357−368.
(15) Huang, Y.; Wang, X.; Paul, D. R. Physical aging of thin glassy polymer films: Free volume interpretation. *J. Membr. Sci.* **2006**, *277* (1), 219−229.
(16) Maillard, D.; et al. Mechanical Properties of Thin Glassy Polymer Films Filled with Spherical Polymer-Grafted Nanoparticles. *Nano Lett.* **2012**, *12*, 3909−3914.
(17) Park, H. B.; et al. Polymers with cavities tuned for fast selective transport of small molecules and ions. *Science* **2007**, *318*, 254−258.
(18) Rittigstein, P.; Torkelson, J. Polymer−nanoparticle interfacial interactions in polymer nanocomposites: confinement effects on glass transition temperature and suppression of physical aging. *J. Polym. Sci., Part B: Polym. Phys.* **2006**, *44* (20), 2935−2943.
(19) Merkel, T. C.; et al. Ultrapermeable, reverse-selective nanocomposite membranes. *Science* **2002**, *296*, 519−522.
(20) Merkel, T. C.; et al. Sorption, transport, and structural evidence for enhanced free volume in poly (4-methyl-2-pentyne)/fumed silica nanocomposite membranes. *Chem. Mater.* **2003**, *15*, 109−123.
(21) Takahashi, S.; Paul, D. R. Gas permeation in poly(ether imide) nanocomposite membranes based on surface-treated silica. Part 1: Without chemical coupling to matrix. *Polymer* **2006**, *47*, 7519−7534.
(22) Hoang, D. T.; Kaufman, L. J.; et al. In situ multi-modal monitoring of solvent vapor swelling in polymer thin films. *Rev. Sci. Instrum.* **2016**, *87* (1), 015106.
(23) Janes, D. W.; Moll, J. F.; Harton, S. E.; Durning, C. J. Dispersion morphology of poly (methyl acrylate)/silica nanocomposites. *Macromolecules* **2011**, *44* (12), 4920−4927.
(24) Fernandes, N. J.; Koerner, H.; Giannelis, E. P.; Vaia, R. A. Hairy nanoparticle assemblies as one-component functional polymer nanocomposites: opportunities and challenges. *MRS Commun.* **2013**, *3*, 13−29.
(25) Budd, P. M.; McKeown, N. B.; et al. Gas separation membranes from polymers of intrinsic microporosity. *J. Membr. Sci.* **2005**, *251* (1), 263−269.
(26) Goyal, S.; Escobedo, F. A. Structure and transport properties of polymer grafted nanoparticles. *J. Chem. Phys.* **2011**, *135* (18), 184902.
(27) Lodge, T. P. Block copolymers: past successes and future challenges. *Macromol. Chem. Phys.* **2003**, *204* (2), 265−273.
(28) Bockstaller, M. R.; Thomas, E. L. Optical properties of polymer-based photonic nanocomposite materials. *J. Phys. Chem. B* **2003**, *107*, 10017−10024.
(29) Voudouris, P.; Choi, J.; et al. Anisotropic elasticity of quasi-one-component polymer nanocomposites. *ACS Nano* **2011**, *5*, 5746−5754.
(30) Barbey, R.; et al. Polymer Brushes via Surface-Initiated Controlled Radical Polymerization: Synthesis, Characterization, Properties, and Applications. *Chem. Rev.* **2009**, *109*, 5437−5527.
(31) Li, C.; et al. A versatile method to prepare RAFT agent anchored substrates and the preparation of PMMA grafted nanoparticles. *Macromolecules* **2006**, *39*, 3175−3183.
(32) Minelli, M.; et al. Oxygen permeability of novel organic-inorganic coatings: I. Effects of organic-inorganic ratio and molecular weight of the organic component. *Eur. Polym. J.* **2008**, *44*, 2581−2588.
(33) Chiou, J. S.; Barlow, J. W.; Paul, D. R. Sorption and transport of gases in miscible poly (methyl acrylate)/poly (epichlorohydrin) blends. *J. Appl. Polym. Sci.* **1985**, *30*, 1173−1186.
(34) Janes, D. W.; Durning, C. J. Sorption and Diffusion of n-Alkyl Acetates in Poly(methyl acrylate)/Silica Nanocomposites. *Macromolecules* **2013**, *46*, 856−866.
(35) Gidley, D. W.; Peng, H. G.; Vallery, R. S. Positron annihilation as a method to characterize porous materials. *Annu. Rev. Mater. Res.* **2006**, *36*, 49−79.
(36) Brunauer, S.; Emmett, P. H.; Teller, E. Adsorption of gases in multimolecular layers. *J. Am. Chem. Soc.* **1938**, *60*, 309−319.
(37) Barrett, E. P.; et al. The determination of pore volume and area distributions in porous substances. I. Computations from nitrogen isotherms. *J. Am. Chem. Soc.* **1951**, *73*, 373−380.
(38) Kremer, K.; Grest, G. S. Dynamics of entangled linear polymer melts: A molecular-dynamics simulation. *J. Chem. Phys.* **1990**, *92*, 5057−5086.
(39) Plimpton, S. Fast parallel algorithms for short-range molecular dynamics. *J. Comput. Phys.* **1995**, *117*, 1−19.
(40) Janes, D. W.; Bilchak, C.; Durning, C. J. Decoupling energetic modifications to diffusion from free volume in polymer/nanoparticle composites. *Soft Matter* **2017**, *13*, 677−685.
(41) Shelley, S. Capturing CO_2: membrane systems move forward. *Chem. Eng. Prog.* **2009**, *105*, 42−47.
(42) Akcora, P.; et al. Gel-like" mechanical reinforcement in polymer nanocomposite melts. *Macromolecules* **2010**, *43*, 1003−1010.
(43) Hansen, J. P.; Verlet, L. Phase Transitions of Lennard-Jones System. *Phys. Rev.* **1969**, *184*, 151.
(44) Agarwal, P.; Qi, H.; Archer, L. A. The ages in a self-suspended nanoparticle liquid. *Nano Lett.* **2010**, *10* (1), 111−115.
(45) Goel, V. Structure of polymer tethered highly grafted nanoparticles. *Macromolecules* **2011**, *44*, 8129−8135.
(46) Morinaga, T.; Ohno, K.; et al. Structural analysis of "Semisoft" colloidal crystals by confocal laser scanning microscopy. *Macromolecules* **2008**, *41*, 3620−3626.
(47) Ohno, K.; et al. Suspensions of silica particles grafted with concentrated polymer brush: a new family of colloidal crystals. *Macromolecules* **2006**, *39*, 1245−1249.
(48) Che, J.; et al. Preparation of Ordered Monolayers of Polymer Grafted Nanoparticles: Impact of Architecture, Concentration, and Substrate Surface Energy. *Macromolecules* **2016**, *49*, 1834−1847.
(49) Hsiao, M.; et al. Microscopic Characterization of Fracture Mechanisms in Polystyrene Grafted Nanoparticle Assemblies: The Role of Film Thickness and Grafting Density. *Microsc. Microanal.* **2016**, *22*, 1856−1857.

DOI: 10.1021/acs.macromol.7b01428
Macromolecules 2017, 50, 7111−7120